Auxiliary material for

S-velocity Model and Inferred Moho Topography beneath the Antarctic Plate from Rayleigh Waves

Meijian An[1], Douglas A. Wiens[2], Yue Zhao[1], Mei Feng[1], Andrew A. Nyblade[3], Masaki Kanao[4], Yuansheng Li[5], Alessia Maggi[6], Jean-Jacques Lévêque[6]

(1, Institute of Geomechanics, Chinese Academy of Geological Sciences, Beijing, China

2, Dept of Earth and Planetary Sci, Washington University, St. Louis MO, USA

3, Dept of Geosciences, Penn State University, University Park, PA, USA

4, National Institute of Polar Research, Tokyo, Japan

5, Polar Research Institute in China, Shanghai, China

6, Institut de Physique du Globe de Strasbourg, Université de Strasbourg/EOST, CNRS, Strasbourg, France)

Journal of Geophysical Research, Solid Earth, 2014

1. Introduction

This file includes four supplementary sections, and captions of 1 supplementary table (Table S1) and 7 figures (Figure S1-S7). Table S1 can be found in "01 Seismic model_ANT_v12_suppl_Table S1_submit.pdf". Figure S1-S7 can be found in respectively in pdf files of figure_S01.pdf, figure_S02.pdf, figure_S03.pdf, figure_S04.pdf, figure_S05.pdf, figure_S06.pdf, figure_S07.pdf.

2. The Antarctic Plate and its Tectonic History

The Antarctic Plate consists of the Antarctic continent and the surrounding oceanic regions. The continent comprises three primary tectonic regions: East Antarctica (EANT), West Antarctica (WANT), and the Transantarctic Mountains. EANT is stable, topographically high, and is thought to feature Precambrian continental lithosphere [*Bentley*, 1991]. In contrast, WANT is an amalgamation of low-lying, younger crustal micro-blocks [*Dalziel and Elliot*, 1982; *Talarico and Kleinschmidt*, 2008].

The Antarctic continent was formed from a number of Archean/Early Proterozoic cratons (older than 1.5 Ga), surrounded by successively younger belts. Amalgamation occurred through accretionary or collisional events, which were episodically punctuated by periods of crustal extension and rifting. The younger belts represent the products of convergent plate tectonic events such as oceanic crust subduction beneath continental crust and/or continent–continent collision [*Talarico and Kleinschmidt*, 2008; *Boger*, 2011].

During the Neoproterozoic, the Rodinia supercontinent is postulated to have formed at ~1.0 Ga and broken apart at ~850–800 Ma [*Torsvik*, 2003]. Within Rodinia, the Mawson craton of East Antarctica was connected with Western Australia [*Fitzsimons*, 2003], making up East Gondwana. East Gondwana was connected with Laurentia

(North America). The northern Prince Charles Mountains, the Napier Complex, Lützow Holm Complex, and Rayner Complex, which are currently part of EANT, were likely connected with India, making up the Indo-Antarctica continent [*Talarico and Kleinschmidt*, 2008; *Torsvik, et al.*, 2008a]. During the break-up of Rodinia, rifting between East Gondwana and Laurentia began at 750–725 Ma [*Dalziel*, 1991]. Prior to 550 Ma, West Gondwana, which consisted of Africa and South America, was connected with the Indo-Antarctica continent. Finally, Gondwana formed when East Gondwana connected with West Gondwana at ~550 Ma [*Boger, et al.*, 2001; *Boger, et al.*, 2002; *Boger*, 2011], see Figure S1a and b. The amalgamation of Gondwana produced the Pan-African orogens, some of the most spectacular mountain-belt building episodes in Earth's history [*Torsvik, et al.*, 2008a]. However, the amalgamation suture zone in EANT (the suture zone marked in Figure S1b is speculated in Boger [2011]) is still not well understood because most of EANT is covered by ice. At ~250 Ma, Gondwana connected with Laurasia to form the most recent supercontinent, Pangaea (see Figure S1c).

Pangaea began breaking apart at 180 Ma. The first major tectonic break-up stage corresponded to an initial rifting phase that started in the Weddell Sea in the Late Jurassic [*Lawver, et al.*, 1991]. This rifting led to the separation of Antarctica from South Africa at ~180 Ma, from India at ~130 Ma, and finally from Australia at ~90 Ma [*Veevers*, 1986; *Torsvik, et al.*, 2008a; *Boger*, 2011], see Figure S2. The separation of

Antarctica from South Africa has been attributed to the Bouvet hotspot [*Hawkesworth, et al.*, 1999; *Torsvik, et al.*, 2008a]. The rifting of Antarctica away from India and then Australia has been attributed to the influence of the Kerguelen hotspot at 140 Ma [*Hawkesworth, et al.*, 1999; *Boger*, 2011]. By ~110 Ma, the micro-plates of West Antarctica had nearly reached their present location with respect to East Antarctica [*Talarico and Kleinschmidt*, 2008]. At ~83 Ma, Antarctica had reached its final polar location and the final break-up was completed when New Zealand rifted away from Marie Byrd Land, WANT [*Stock and Molnar*, 1987; *Lawver, et al.*, 1991; *Larter, et al.*, 2002; *Torsvik, et al.*, 2008b]. After break-up was complete, geological activity in Antarctica was limited to on-going extension and volcanism in the West Antarctic Rift System (WARS). Given Antarctica's shared tectonic history with neighboring Gondwanan continents (e.g., Africa, India, Australia, Zealandia, and South America), geological and tectonic similarities naturally exist along and close to the continent boundaries [*Gohl*, 2008].

During the tectonic history of Antarctica, all blocks of EANT were amalgamated at ~500 Ma, while WANT, and the whole of Antarctica, were amalgamated at ~110 Ma. For a significant period of Earth's history, Antarctica has held a central position within both the supercontinents of Rodinia (1300–700 Ma) and Gondwana (550–200 Ma) [*Dalziel*, 1991; *Moores*, 1991; *Talarico and Kleinschmidt*, 2008]. The current Antarctic plate was formed primarily during the formation of the Gondwanan supercontinent, especially during three main periods: (1) c. 600–450 Ma, during the amalgamation of Gondwana; (2) c. 450–180 Ma, from the end of Gondwanan amalgamation to the onset of break-up; and (3) c. 180–0 Ma, since the break-up of Gondwana. The geology of the Antarctic continent, particularly the EANT, was established during the first two periods [*Talarico and Kleinschmidt*, 2008]. During the third period, the oceanic region was formed and WANT was re-formed [*Torsvik, et al.*, 2008a].

3. 3D S-velocity model inversion from surface wave dispersion

For waves with a period of P_j, the wave propagation path of the *k-th* ray can be discretized and its travel time (t_k) expressed as:

$$t_k = \boldsymbol{G}_k \cdot \boldsymbol{S} \tag{1}$$

where $\boldsymbol{G}_k$ is a row of the observation matrix $\boldsymbol{G}$ with *k-th* path segment lengths for each discretized cell and $\boldsymbol{S}$ is the surface-wave group/phase slowness (reciprocal of velocity) vector. The relationship between the slowness $S(P_j)$ of the period P_j and the perturbation of *S*-velocity ($\Delta\beta_i$) of the *i-th* layer in a vertical S-velocity model where the wave propagates can be written as:

$$S(P_j) = S_{\mathrm{Ref}}(P_j) + \sum_{i=1}^{n} \frac{\partial S}{\partial \beta_i} \Delta\beta_i \tag{2}$$

where $S_{\mathrm{Ref}}(P_j)$ is the group/phase slowness of a given reference model and $\partial S/\partial\beta_i$ is the partial derivative of the group/phase slowness to the *S*-velocity of the *i-th* layer in the reference model. Replacing the vector $\boldsymbol{S}$ in Eq. (1) by the slowness in Eq. (2), changes

Eq. (1) to:

$$t_k = \boldsymbol{A}_k \cdot \boldsymbol{B} + c_k \tag{3}$$

where $\boldsymbol{A}_k$ is a coefficient matrix deduced from operations between matrix $\boldsymbol{G}_k$ and all partial derivatives $\partial S/\partial \beta_i$, $\boldsymbol{B}$ is the vector of 3-D S-velocity perturbations to be determined, and c_k is a constant obtained from the combination of $\boldsymbol{G}_k$ and $S_{\mathrm{Ref}}(P_j)$. For all paths and periods, we can then obtain the travel time vector ($\boldsymbol{T}$) in the following matrix form:

$$\boldsymbol{T} = \boldsymbol{A} \cdot \boldsymbol{B} + \boldsymbol{C} \tag{4}$$

where $\boldsymbol{C}$ (= c_1, …, c_k, …) is a constant vector. Because Eq. (4) is commonly ill posed, we used the 3D first-order spatial gradient (∇) of the model as an *a priori* constraint, and the final inversion equation then becomes:

$$\begin{pmatrix} \boldsymbol{T} - \boldsymbol{C} \\ \boldsymbol{0} \end{pmatrix} = \begin{pmatrix} \boldsymbol{A} \\ \lambda \nabla \end{pmatrix} \cdot \boldsymbol{B} \tag{5}$$

where λ is a weighting factor to balance between fitting of the travel times and model smoothing. The above equations show that our inversion for S-velocities is a linearized inversion combining a horizontal 2D surface wave dispersion linear inversion and a vertical 1D linearized inversion. A detailed description of this method can be found in *Feng and An* [2010].

4. Spatial resolution analysis

Resolution lengths of an inverse problem can be retrieved from a resolution matrix that defines a linear projection [*Nolet*, 2008; *Thurber and Ritsema*, 2009; *An*, 2012]. Our tomographic inversion for a 3D S-velocity model is, in fact, a linearized inversion, and a resolution matrix can be outputted at any iteration for a linearized inversion. However, the matrix cannot give the expected resolution lengths of the final model, but only an approximate resolution length for a model with respect to a given reference model. The real model resolution length will depend not only on the reference model, but also on the nonlinearity of the observation operator in the inverse problem [*An*, 2012]. Therefore, we do not provide quantitative resolution lengths from the resolution matrix of the 3D S-velocity inversion. However, we present quantitative resolution lengths for the horizontal 2D surface wave dispersions, which are useful in evaluating the lateral resolution of a surface wave study. The lateral resolution lengths were retrieved by using the statistical resolution length calculation proposed by *An* [2012]. Visualization of the inverted solution model from a random synthetic model cannot only yield resolution length information, but also the direction dependence of the resolution [*An*, 2012]. Therefore, in addition to the statistical resolution analyses for the dispersions, we also analyzed the lateral and vertical resolution from visualization of the inverted 3D output model using random synthetic 3D input models, based on all the rays of real observations.

A statistical resolution analysis is simple and independent of the approach and parameterization used in the inversion. The statistical resolution length calculation includes two steps. The first step is to create a random synthetic input model, and then to obtain an output solution using the input model as in a general synthetic test. The second step is to invert for resolution lengths for all model parameters. A detailed introduction to these procedures can be found in *An* [2012]. Figure S3c–e shows the resolution length distribution for the Rayleigh wave dispersion at periods of 50, 100, and 150 s. This figure shows that the horizontal resolution length of the whole continent can be ~100 km for a period of 50 s and ~250 km for a period of 150 s, and in the oceanic areas are ~200 and ~500 km, respectively.

As described above, it is not possible to obtain a resolution length for the 3D model as the inversion is nonlinear, and it is also difficult to determine indicative resolution information by checkerboard tests given the complexity of the model parameterization. However, a simple method can be used to provide indicative resolution information for the 3D model. *An* [2012] noted that even for a random synthetic input model without specific checkers, an inverse output solution can yield an anomaly pattern similar to the output of a checkerboard test, which can provide not only resolution length information but also the direction dependence of the resolution. A synthetic random model and its solution used in the above statistical resolution analysis to give the lateral resolution length for a 2D dispersion inversion are shown in Figure S3a and b. In this figure, even though the inverted solution (Figure S3b) depends on the random synthetic model (Figure S3a), the solution not only visually provides resolution length information, but also the direction dependence of the resolution length. In Figure S3b, most of the anomaly pattern appears as a strip with a long axis along the meridian and a short axis along the line of the latitude, particularly for the oceanic region where the anomaly patterns in the input synthetic model (Figure S3a) have little similarity to the strip anomaly in the solution (Figure S3b). This anomaly pattern indicates that the resolution length along the meridian is larger than that along the line of latitude. Given that most of the observation stations are located inside continental Antarctica and that the earthquakes are coming from the plate boundaries (Figure 1), the rays should mainly intersect at positions far from the plate boundary and the rays at positions close to the plate boundary are largely parallel to neighboring rays. In practice, the resolution length along the parallel direction (i.e., almost parallel to meridian) of the rays should be greater than in the normal direction (i.e., almost parallel to the line of latitude), which is consistent with the indicative example of an inverted solution in Figure S3b.

A visualization of an inverted solution model from a random synthetic model cannot only provide indicative resolution length information, but also the direction dependence of the resolution. As such, we have also indicatively analyzed the lateral and vertical resolution from a visualization of the inverted 3D solution using random synthetic 3D models, based on real ray observations. We created several random synthetic 3D S-velocity models, and obtained the solutions by inverting the synthetic observations from the synthetic models. Figure S4 shows horizontal slices of an inverted 3D S-velocity solution from one of these random synthetic 3D models. The solution slices at depths of 50, 120, and 200 km (Figure S4b–d) demonstrate not only direction dependence of the resolution in the oceanic region, similar to those implied from Figure S3, but also depth dependence. It should be noted that the inverted solution of any random model depends on the synthetic model and, therefore, only one inverted solution from a random synthetic model cannot provide full resolution length information for the whole area. Given that we only show one solution model here, we selected a model that indicatively provides resolution length information for a typical region (e.g., GSM). Beneath the region close to the GSM, the checker-like anomaly extent is at a minimum of ~250 km at depths of 50 km (Figure S4b), ~500 km at depths of 120 km (Figure S4c), and ~800 km at depths of 200 km (Figure S4d). This indicates that the horizontal resolution length is ~120 km at a depth of 50 km, ~250 km at a depth of 120 km, and ~400 km at a depth of 200 km beneath the GSM. In the oceanic region close to Marie Byrd Land (MBL), the extent of the checker-like anomaly at a depth of 50 km (Figure S4b) is ~300 km along the short axis and ~1000 km in a direction close to meridian, which indicates that the resolution length at a depth of 50 km is ~150 km along the line of latitude and ~500 km along the meridian. The checker-like anomaly extent is ~1000 km at a depth of 120 km and ~1500 km at a depth of 200 km, which indicates that the resolution length is ~500 km at a depth of 120 km and ~750 km at a depth of 200 km.

The two vertical slices shown in Figure S4e and f indicate that the vertical and horizontal resolution length increases with increasing depth, as expected from sensitivity of surface wave dispersion with respect to S-velocities (Figure S5). Beneath the GSM, the vertical extents of the anomalies in this figure are ~20 km down to 60 km, ~50 km down to 150 km, and ~100 km down to 250 km, which indicates that the vertical resolution lengths are ~10 km down to 60 km, ~25 km down to 150 km, and ~50 km down to 250 km. The discontinuity in the resolution length should be greater than that of the velocity model [*An*, 2012], and the vertical resolution length for the Moho depth retrieved from the 3D model should be <10 km, because the Moho depth is mostly <60 km, and for the seismic lithosphere–asthenosphere boundary (LAB) should be smaller than 25–50 km, because LAB is mostly at the depths of ~100–250 km.

5. Antarctic Moho Compilation of AN-Moho

We compiled crustal thicknesses and/or Moho depths (Figure S7a) from active seismic and receiver function studies, and constructed a crustal thickness compilation of ANtarctic Moho positions (AN-Moho; Figure S7c). Even though previous surface wave studies yielded average crustal thicknesses over a large area, we did not compile these crustal thicknesses.

Using Moho depths beneath scatter points, *Baranov and Morelli* [2013] assembled a

Moho model by kriging interpolation without quality discrimination for Moho depths published prior to 2012. We have made three improvements over the compilation of Moho depths by *Baranov and Morelli* [2013]. First, we included new data collected after 2012. For example, Moho depths from PRF analyses beneath POLENET stations in WANT [*Chaput, et al.*, 2014] and from SRF analyses beneath six Chinese EANT stations [*Feng, et al.*, 2014] at locations where the Moho had not been previously studied were used here. Second, we evaluated the quality of obtained Moho depths from the original publications, and discarded poor data with large uncertainties due to the quality of the observations. For example, we selected Moho depths obtained beneath TransAntarctic Mountains Seismic Experiment (TAMSEIS) stations over the ice sheet from *Hansen, et al.* [2009], but not from *Lawrence, et al.* [2006], which was used in *Baranov and Morelli* [2013]. Third, we corrected all thicknesses using the same definition of crustal thickness. Therefore, slight differences exist between the data for AN-Moho as compared with the previous compilation and also the data presented in the original publications. More details of these screening procedures and thickness corrections are described below.

The crustal thickness or Moho depth data presented in different publications may use different definitions, which can result in different crustal thickness values beneath the same position. In most RF studies, crustal thickness is defined as the distance from the solid surface to the Moho, and the ice thickness is included in the crustal thickness.

However, Hansen et al. [2009; 2010] and Chaput et al. [2014] defined the crustal bedrock thickness as representing the crustal thickness, which does not include the ice thickness. In active-source seismic studies, crustal thickness is often defined as the distance from sea level to the Moho. We defined crustal thickness as the distance from the uppermost solid (i.e., ice, sediment, or bedrock) surface to the Moho discontinuity, and the Moho depth as being from sea level to the Moho discontinuity. If a previous study presented surface elevation data, we used the given elevation in the conversion between crustal thickness and Moho depth. Otherwise, the solid surface elevation from ETOPO2 was used in the conversion. We corrected all the thicknesses or depths in previous studies in this fashion. After the conversion, different crustal thickness values may yield the same information. For example, at the station BYRD, the crustal thickness converted from the result (24.3 km) of Chaput et al. [2014] becomes 26.75 km, which is essentially the same as the value of 27 km of Winberry and Anandakrishnan [2004].

Crustal thickness can be measured by several types of seismic observations, and even one observation may yield different crustal thicknesses depending on the analytical method applied to the data. Some observations or analytical methods may result in large uncertainties. Therefore, the crustal thicknesses given in previous studies may vary significantly for the same position. Where two or more publications provided crustal thickness data for the same location, we calculated the differences between these data for each position, and all crustal thicknesses with a difference of >2 km are shown in Figure S7b. This figure shows that the difference between crustal thicknesses given by different publications can be as large as ~10 km. In Figure S7b, the differences are most evident at: (1) between the SRF [*Hansen, et al.*, 2009; *Hansen, et al.*, 2010] and PRF results [*Lawrence, et al.*, 2006; *Finotello, et al.*, 2011]; and (2) between the PRF results of *Finotello, et al.* [2011] and *Lawrence, et al.* [2006] and those of the DRV station from *Kanao and Shibutani* [2012] and *Reading* [2004]. In addition to the crustal thicknesses for the stations listed in Figure S7b, crustal thickness data from only one publication may also have a large uncertainty. Therefore, we discarded data with large uncertainties that reflect both the observation quality and analytical method, as outlined below.

PRF analysis has become a general method to rapidly and simply provide a crustal thickness, and SRF analyses have also been recently used to obtain crustal thickness data. Generally, the signal-to-noise ratio of the first-arriving P-wave is higher than that of the secondary phase or S-wave, and the wavelength of the PRF is much shorter than that of the SRF, because the signal frequencies used in a PRF study are typically higher than those used in a SRF study. Therefore, a Moho depth obtained from a PRF should have a better resolution than that from a SRF. As such, for land stations where the difference between the SRF and PRF results was large, we used the PRF results. For example, we selected data from *Lawrence, et al.* [2006] rather than *Hansen, et al.*

[2009] for onland stations (E000–E010 and coastal stations). However, for seismic stations over the ice cap, the ice is so thick that it influences the PRF more than the SRF. The PRF analysis of *Lawrence, et al.* [2006] did not account properly for the ice sheet and as such the results are poor for stations on the ice sheet [*Hansen, et al.*, 2009] (i.e., E012–E030 and all N stations). Given this, we selected crustal thickness data from the SRF analyses of *Hansen, et al.* [2009], but not from the PRF analyses of *Lawrence, et al.* [2006].

An unclear Ps phase in the PRF or Sp phase in the SRF indicates that the Moho discontinuity is not sharp, and the resulting Moho depth from the receiver function may have a large uncertainty. For example, two different Moho depths of 42 km [*Reading*, 2004] and 28 km [*Kanao and Shibutani*, 2012] for the station DRV (Figure S7b) were estimated from inverted S-velocity models by PRF waveforms with an unclear Ps phase.

After an RF waveform is obtained, a Moho depth can be obtained by various methods [e.g., *Ammon, et al.*, 1990; *Zhu and Kanamori*, 2000; *Chaput, et al.*, 2014]. However, different methods may result in different calculated Moho depths. For example, the Moho estimated from a 1D multi-layer S-velocity model inverted from the receiver function [e.g., *Ammon, et al.*, 1990] may be different with that directly measured by the H–κ stacking method assuming a constant Vp and single crustal layer [*Zhu and*

Kanamori, 2000]. The differences between *Lawrence, et al.* [2006] and *Finotello, et al.* [2011], reflect the fact that *Lawrence, et al.* [2006] used the first method, whereas *Finotello, et al.* [2011] used the second method. The differences for some coastal stations, such as CBOB, also can be interpreted as that which interface was identified as the Moho differs [*Finotello, et al.*, 2011]. For example, *Lawrence, et al.* [2006] associated a velocity jump from ~3.45 to 4.1 km/s as the Moho, whereas *Finotello, et al.* [2011] associated the Moho with a velocity jump from 4.1 to 4.45 km/s. It is well known that the Moho represents a sharp increase from a low velocity in the crust to a high velocity in upper mantle. However, during the procedure of inverting 1D S-velocities from receiver functions, vertical smearing or smoothing will result in a lower S-velocity at the real Moho position in the inverted model than the real structure. As such, it is reasonable to select a velocity slightly lower than expected for the upper mantle to represent the velocity at the Moho position. Furthermore, the velocity increase with depth from 3.45 to 4.1 km/s in *Lawrence, et al.* [2006] is sharper than that from 4.1 km/s to 4.45 km/s, which indicates that the Moho position is at the shallower of the two estimates. For a complex crustal structure like that beneath CBOB, the assumption of both a constant Vp and single layer model used in the H–κ stacking method may be too simplistic, and can result in a large uncertainty on the calculated crustal thickness. For example, S-velocity models beneath SBA [*Bannister, et al.*, 2003] show that Vs gradually increases from 1.2 to 4.3 km/s down to 20 km, which implies that Vp is also gradually increasing through these depths. In this case, a constant Vp and single layer model used in the H–κ stacking method may not adequately represent the structure beneath SBA. Receiver functions from different studies [*Bannister, et al.*, 2003; *Lawrence, et al.*, 2006; *Finotello, et al.*, 2011] are similar and provide a similar time difference between Ps and P of ~4 s. However, *Finotello, et al.* [2011] calculated a 27 km deep Moho by the H–κ stacking method, and S-velocity models inverted by two different global algorithms by *Bannister, et al.* [2003] and *Lawrence, et al.* [2006] both yielded different thickness of ~21 km. Similar issues can also be identified for other stations, such as CBOB, CTEA, CCRZ (CCRI in Table 1 of *Lawrence, et al.* [2006], and MAGL. For the above reasons, we discarded the Moho depths from *Finotello, et al.* [2011] and those obtained using S-velocity model inversions in other studies.

For the SNAA station, *Bayer, et al.* [2009] obtained a 41-km-thick crust, corresponding to a high Vp/Vs from the H–κ method, and also calculated a 39-km-thick crust from the time difference between Ps and P. We used the mean of the two thicknesses (40 km), which is also the Moho depth estimated from short-period (2–12 s) signals [see Table 4 in *Bayer, et al.*, 2009]. The Moho depth of 52 km for MUCs is from MUC6–8 stations and of 45 km for AWIs is from AWI2–4 of fig. 10 in *Bayer, et al.* [2009].

The names of some positions have been modified according to the information in original publications. J99-S1 to J99-S6 are shot points from S1 to S6, respectively, of the 41st Japanese Antarctic Research Expedition (JARE41) in the austral summer of

1991–2000 [*Yoshii, et al.*, 2004], and J01-SPs are SP1–SP7 of JARE43 in the 2001–2002 season [*Miyamachi, et al.*, 2003]. J01-SP3 and 4 were discarded because the locations are too close and give the same Moho depth as J99-S3. WA-As or WA-Bs are sections A and B, respectively, from the Wilkes–Adelie margin of Antarctica [*Eittreim*, 1994]. M450 is the mid-point between shots 45 and 50 of the reflection profile from[*McGinnis, et al.*, 1985]. The numbers for the points from D000 to D780 represent the distance along the profile in fig. 5 of *Leitchenkov and Kudryavtzev* [1997]. RIS51 and 56 are stations 51 and 56 on the Ronne Ice shelf from *Jokat, et al.* [1997]. Fisher is the FISH station from Reading [2006].

On the basis of the above corrections and selection criteria, we compiled the AN-Moho (Figure S7c) and Moho depths listed in Table S1. Apart from the crustal thickness of Dome F (Figure S7a) obtained from gravity data in *Kanao, et al.* [2012], no valid data from seismic methods is yet available for Queen Maud Land (QML), Dome F, and Ellsworth Land (EL). In our compilation, most of the Moho points in the AN-Moho are located on the Antarctic continent. The thickest crust is found beneath Dome A, where it is as thick as ~61.6 km, whereas the Moho is 57.5 km below sea level. For oceanic regions, the oceanic crust is generally thin (average thickness, ~6 km; [*McClain and Atallah*, 1986]. However, several measurements of oceanic crustal thickness around Antarctica where ocean depths are >3 km have shown that the crustal thickness varies in the range of 7–20 km. Therefore, the oceanic crustal structure around Antarctica is complex.

References

Ammon, C. J., G. E. Randall, G. Zandt (1990), On the nonuniqueness of receiver function inversions, *J. Geophys. Res.*, *95*, 15303-15318.

An, M. (2012), A simple method for determining the spatial resolution of a general inverse problem, *Geophys. J. Int.*, *191*, 849-864.

Bannister, S., J. Yu, B. Leitner, B. L. N. Kennett (2003), Variations in crustal structure across the transition from West to East Antarctica, Southern Victoria Land, *Geophysical Journal International*, *155*, 870-880.

Baranov, A., A. Morelli (2013), The Moho depth map of the Antarctica region, *Tectonophysics*, *609*, 299-313.

Bayer, B., W. H. Geissler, A. Eckstaller, W. Jokat (2009), Seismic imaging of the crust beneath Dronning Maud Land, East Antarctica, *Geophysical Journal International*, *178*, 860-876.

Bentley, C. R. (1991), Configuration and structure of the subglacial crust, in *The Geology of Antarctica*, edited by R. J. Tingey, pp. 335-364, Clarendon, Oxford.

Boger, S. D., C. J. L. Wilson, C. M. Fanning (2001), Early Paleozoic tectonism within the East Antarctic craton: The final suture between east and west Gondwana?, *Geology*, *29*, 463-466.

Boger, S. D., C. J. Carson, C. M. Fanning, J. M. Hergt, C. J. L. Wilson, J. D. Woodhead (2002), Pan-African intraplate deformation in the northern Prince Charles Mountains, east Antarctica, *Earth and Planetary Science Letters*, *195*, 195-210.

Boger, S. D. (2011), Antarctica — Before and after Gondwana, *Gondwana Research*, *19*, 335-371.

Breitsprecher, K., D. J. Thorkelson (2009), Neogene kinematic history of Nazca–Antarctic–Phoenix slab windows beneath Patagonia and the Antarctic Peninsula, *Tectonophysics*, *464*, 10-20.

Chaput, J., R. C. Aster, A. Huerta, X. Sun, A. Lloyd, D. Wiens, A. Nyblade, S.

Anandakrishnan, J. P. Winberry, T. Wilson (2014), The crustal thickness of West Antarctica, *Journal of Geophysical Research: Solid Earth*, *119*, 378-395.

Dalziel, I. W. D., D. H. Elliot (1982), West Antarctica: Problem child of Gondwanaland, *Tectonics*, *1*, 3-19.

Dalziel, I. W. D. (1991), Pacific margins of Laurentia and East Antarctica-Australia as a conjugate rift pair: Evidence and implications for an Eocambrian supercontinent, *Geology*, *19*, 598-601.

Eittreim, S. L. (1994), Transition from continental to oceanic crust on the Wilkes-Adelie margin of Antarctica, *Journal of Geophysical Research: Solid Earth*, *99*, 24189-24205.

Feng, M., M. An (2010), Lithospheric structure of the Chinese mainland determined from joint inversion of regional and teleseismic Rayleigh-wave group velocities, *J. Geophys. Res.*, *115*, B06317.

Feng, M., M. An, C. An, G. Shi, Y. Zhao, Y. Li, D. Wiens (2014), Crustal Thicknesses along the Traverse from Zhongshan to Dome A in Eastern Antarctica, *Chinese J. Polar Research*, *26*, 177-185.

Finotello, M., A. Nyblade, J. Julia, D. Wiens, S. Anandakrishnan (2011), Crustal Vp–Vs ratios and thickness for Ross Island and the Transantarctic Mountain front, Antarctica, *Geophysical Journal International*, *185*, 85-92.

Fitzsimons, I. C. W. (2003), Proterozoic basement provinces of southern and southwestern Australia, and their correlation with Antarctica, *Geological Society, London, Special Publications*, *206*, 93-130.

Gohl, K. (2008), Antarctica's Continent-Ocean Transitions: Consequences for Tectonic Reconstructions, in *Antarctica: A Keystone in a Changing World —Online Proceedings of the 10th International Symposium on Antarctic Earth Sciences.*, edited by A. K. Cooper, et al., p. kp04, The National Academies Press, Washington, DC.

Hansen, S. E., J. Julià, A. A. Nyblade, M. L. Pyle, D. A. Wiens, S. Anandakrishnan

(2009), Using S wave receiver functions to estimate crustal structure beneath ice sheets: An application to the Transantarctic Mountains and East Antarctic craton, *Geochem. Geophys. Geosyst.*, *10*, Q08014.

Hansen, S. E., A. A. Nyblade, D. S. Heeszel, D. A. Wiens, P. Shore, M. Kanao (2010), Crustal structure of the Gamburtsev Mountains, East Antarctica, from S-wave receiver functions and Rayleigh wave phase velocities, *Earth and Planetary Science Letters*, *300*, 395-401.

Hawkesworth, C., S. Kelley, S. Turner, A. Le Roex, B. Storey (1999), Mantle processes during Gondwana break-up and dispersal, *Journal of African Earth Sciences*, *28*, 239-261.

Jokat, W., N. Fechner, M. Studinger (1997), Geodynamic models of the Weddell Sea embayment in view of new geophysical data, in *The Antarctic Region: Geological Evolution and Processes*, edited by C. A. Ricci, pp. 453-459, Terra Antartica Publication, Siena, Italy.

Kanao, M., S. E. Hansen, K. Kamiyama, D. Wiens, T. Higashi, A. A. Nyblade, A. Watanabe (2012), Crustal structure from the Lützow-Holm Bay to the inland plateau of East Antarctica, based on onshore gravity surveys and broadband seismic deployments, *Tectonophysics*, *572–573*, 100-110.

Kanao, M., T. Shibutani (2012), Shear Wave Velocity Models Beneath Antarctic Margins Inverted by Genetic Algorithm for Teleseismic Receiver Functions, in *Seismic Waves - Research and Analysis*, edited by M. Kanao, pp. 237-252, InTech.

Kennett, B. L. N., E. R. Engdahl (1991), Traveltimes for global earthquake location and phase identification, *Geophys. J. Int.*, *105*, 429-465.

Larter, R. D., A. P. Cunningham, P. F. Barker, K. Gohl, F. O. Nitsche (2002), Tectonic evolution of the Pacific margin of Antarctica 1. Late Cretaceous tectonic reconstructions, *Journal of Geophysical Research: Solid Earth*, *107*, 2345.

Lawrence, J. F., D. A. Wiens, A. A. Nyblade, S. Anandakrishnan, P. J. Shore, D. Voigt

(2006), Crust and upper mantle structure of the Transantarctic Mountains and surrounding regions from receiver functions, surface waves, and gravity: Implications for uplift models, *Geochem. Geophys. Geosyst.*, *7*, Q10011.

Lawver, L. A., J.-Y. Royer, D. A. Sandwell, C. T. Scotese (1991), Evolution of the Antarctic continental margins, in *Geological Evolution of Antarctica*, edited by M. R. A. Thomson, et al., pp. 533-539, Cambridge University Press, Cambridge.

Leitchenkov, G., G. Kudryavtzev (1997), Structure and origin of the Earth's Crust in the Weddell Sea Embayment (beneath the Front of the Filehner and Ronne lee Shelves) from deep seismic sounding data, *Polarforschung*, *67*, 143-154.

McClain, J. S., C. A. Atallah (1986), Thickening of the oceanic crust with age, *Geology*, *14*, 574-576.

McGinnis, L. D., R. H. Bowen, J. M. Erickson, B. J. Allred, J. L. Kreamer (1985), East-West Antarctic boundary in McMurdo sound, *Tectonophysics*, *114*, 341-356.

Miyamachi, H., S. Toda, T. Matsushima, M. Takada, A. Watanabe, M. Yamashita, M. Kanao (2003), A refraction and wide-angle reflection seismic exploration in JARE-43 on the Mizuho Plateau, East Antarctica, *Polar Geoscience*, *16*, 1-21.

Moores, E. M. (1991), Southwest U.S.-East Antarctic (SWEAT) connection: A hypothesis, *Geology*, *19*, 425-428.

Nolet, G. (2008), *A breviary of seismic tomography: imaging the interior of the earth and sun*, Cambridge University Press, Cambridge, UK.

Reading, A. M. (2004), The Seismic Structure of Wilkes Land/Terre Adelie, East Antarctica and Comparison with Australia: First Steps in Reconstructing the Deep Lithosphere of Gondwana, *Gondwana Research*, *7*, 21-30.

Reading, A. M. (2006), The seismic structure of Precambrian and early Palaeozoic terranes in the Lambert Glacier region, East Antarctica, *Earth and Planetary Science Letters*, *244*, 44-57.

Schettino, A., C. R. Scotese (2005), Apparent polar wander paths for the major continents (200 Ma to the present day): a palaeomagnetic reference frame for global plate tectonic reconstructions, *Geophysical Journal International*, *163*, 727-759.

Stock, J., P. Molnar (1987), Revised history of early Tertiary plate motion in the south-west Pacific, *Nature*, *325*, 495-499.

Talarico, F. M., G. Kleinschmidt (2008), Chapter 7 The Antarctic Continent in Gondwanaland: A Tectonic Review and Potential Research Targets for Future Investigations, in *Antarctic Climate Evolution*, edited by F. Fabio and S. Martin, pp. 257-308, Elsevier.

Thurber, C. H., J. Ritsema (2009), Theory and Observations - Seismic Tomography and Inversion Methods, in *Treatise on Geophysics: Seismology and Structure of the Earth*, edited by B. Romanowicz and A. Dziewonski, pp. 323-360, Elsevier, Amsterdam, the Netherlands.

Torsvik, T. H. (2003), The Rodinia Jigsaw Puzzle, *Science*, *300*, 1379-1381.

Torsvik, T. H., C. Gaina, T. F. Redfield (2008a), Antarctica and Global Paleogeography: From Rodinia, Through Gondwanaland and Pangea, to the Birth of the Southern Ocean and the Opening of Gateways, in *Antarctica: A Keystone in a Changing World —Online Proceedings of the 10th International Symposium on Antarctic Earth Sciences.*, edited by A. K. Cooper, et al., p. kp11, The National Academies Press, Washington, DC.

Torsvik, T. H., R. D. Müller, R. Van der Voo, B. Steinberger, C. Gaina (2008b), Global plate motion frames: Toward a unified model, *Reviews of Geophysics*, *46*, RG3004.

Veevers, J. J. (1986), Breakup of Australia and Antarctica estimated as mid-Cretaceous (95 ± 5 Ma) from magnetic and seismic data at the continental margin, *Earth and Planetary Science Letters*, *77*, 91-99.

Winberry, J. P., S. Anandakrishnan (2004), Crustal structure of the West Antarctic rift system and Marie Byrd Land hotspot, *Geology*, *32*, 977-980.

Yoshii, K., K. Ito, H. Miyamachi, M. Kanao (2004), Crustal structure derived from refractions and wide-angle reflections in the Mizuho Plateau, East Antarctica, *Polar Geoscience*, *17*, 112-138.

Zhu, L., H. Kanamori (2000), Moho depth variation in southern California from teleseismic receiver functions, *Journal of Geophysical Research: Solid Earth*, *105*, 2969-2980.

Caption of supplementary table:

Table S1. Crustal thicknesses in the compilation of AN-Moho

(This table can be found in “01 Seismic model_ANT_v12_suppl_Table S1_submit.pdf”)

Captions of supplementary figures:

Figure S1 Illustration of the progressive formation of Gondwana and Pangaea. The formation steps of Gondwana in (a, b) are simplified from [*Boger*, 2011]. The reconstruction of Pangaea in (c) is from [*Schettino and Scotese*, 2005]. AF = African continent; AU = Australian continent; EANT = East Antarctica; IN = Indian continent; SA = South American continent. A red circle labeled with "A" marks the position of Dome Argus of the GSM, which is the highest ice feature in Antarctica. Three rectangles labeled with a number highlight typical areas of EANT which were respectively parts of three continents (1: West Gondwana; 2: Indo-Antarctica; 3: East Gondwana). Blue arrows indicate the movement or rotation of the continent. The block shaded by yellow color has not been geologically studied. Red dashes in (b) indicatively mark suture zone of the amalgamation of the three continents, and in (c) mark the boundary of Gondawana.

Figure S2 Illustration of the evolution of Gondwana during the past 160 Ma. AF = African continent; AP = Antarctic Peninsular; AUS = Australian continent; BaH = Balleny hotspot; BH = Bouvet hotspot; EANT = East Antarctica; IN = Indian continent; KH = Kerguelen hotspot; MH = Marion hotspot; SA = South American continent. The continental reconstructions and the locations of LIPs are from [*Schettino and Scotese*, 2005]. The subduction zones shown in panels (a) to (c) are adapted from [*Torsvik, et al.*, 2008a], and in (d) are from [*Breitsprecher and Thorkelson*, 2009]. The hotspots of BH, MH, and KH are from [*Torsvik, et al.*, 2008a].

Figure S3. Resolution length information for Rayleigh wave dispersions at periods of (a–c) 50 s, (d) 100 s, and (e) 150 s. Plate (b) shows the inverted solution for a synthetic model in (a) at a period of 50 s. The resolution length maps (c–e) were retrieved from 400 pairs of random synthetic models and their solutions. The propagation paths used to estimate the resolution lengths in (c–e) are the same as those in Figure 3b–d.

Figure S4. The 3D S-velocity solutions directly inverted from the synthetic observations of random synthetic models. (a) is a slice of a random synthetic model at a depth of 50 km. (b) and (c) are slices at depths of 50 and 120 km, respectively and (e) and (f) are vertical slices along two transects, respectively, however, the slices and transects are from the same solution inverted from the synthetic 3D model shown in (a). (d) is a slice at a depth of 200 km from a solution on the basis of another random synthetic model.

Figure S5. Fundamental-mode Rayleigh wave group velocity (U) sensitivity with respected to vertical S-velocity (β) variation at depth. The sensitivities are calculated on the basis of IASPEI91 model [Kennett and Engdahl, 1991].

Figure S6. Two 3D models from inversions with and without Moho constraints in the last iteration. The 1D profiles in (b) are beneath the same position labeled with “t” in (a), in which the position of the transect A-A’ in (c) and (d) is also shown. The symbols in (c,d) are the same as those in Figure 7.

Figure S7. Moho depths. (a) Positions (plus symbol) of Moho depths from previous studies. (b) Moho depths with a difference of >2 km at a given position. The points surrounded by black lines were used in the AN-Moho model. (c) Moho depths in the compilation of AN-Moho for Antarctica. All the Moho depths and the previous studies that the Moho depths come from are listed in Table S1.

Table S1 Crustal thicknesses in the compilation of AN-Moho

Name	Longitude (°)	Latitude (°)	Crustal thickness (km)	Moho depths (km)	Sources
9169	-6.02	-75	45.0	42.3	1
9172	-9.7	-73.6	44.0	42.6	1
96100B	5.9	-67.7	12.0	16.0	2
96100E	6.1	-69.7	23.0	25.0	2
96110B	-14.1	-69	10.0	14.0	2
96110E	-12.5	-73.5	21.0	23.0	2
A	67	-72	32.0	32.0	3,4
AMERY	73.85	-69.71	30.0	30.0	3,4
AN01	166.92	-77.19	20.0	19.8	5
AN05	163.96	-77.69	18.0	17.8	5
AN08	160.15	-77.54	40.0	37.9	5
AN09	162.17	-77.93	34.0	32.8	5
AN10	162.83	-77.63	32.0	31.3	5
AWI2-4	-13.09	-74.5	45.9	45.0	6
B	78.2	-68.77	34.0	34.0	3,4
BEAVER	68.34	-70.75	30.0	30.0	3,4
BT01	166.563	-71.112	25.0	23.3	7
BT05	158.928	-69.89	31.0	29.5	7
BT06	157.337	-69.514	32.0	31.4	7
BT07	155.03	-69.245	31.0	30.0	7
BVLK	68.17	-70.8	33.0	32.9	8
BYRD	-119.473	-80.0168	26.75	25.2	9
BYRD	-119.5466	-80	27.0	25.5	10
C	69.09	-71.55	24.0	24.0	3,4
CASE	160.1262	-80.4481	27.8	27.0	11
CASEY	110.31	-66.17	30.0	30.0	12
CBOB	163.1707	-77.0342	20.1	20.0	11
CBRI	166.4266	-77.2516	18.3	18.0	11
CCRZ	169.0947	-77.5166	19.8	19.0	11
CHNA	77.013	-78.677	46.8	43.3	13
CHNB	76.976	-77.1744	57.5	54.5	13
CLRK	-141.8485	-77.3231	30	29.0	9
CPHI	162.6484	-75.0745	22.2	22.0	11
CRES	64.17	-72.66	33.0	31.6	8
CTEA	160.7643	-78.9439	21.3	20.0	11
D000	298.5	-74.86	37.0	37.0	14
D100	301	-75.45	35.0	35.0	14
D200	304	-76.06	33.0	33.0	14

D320	-52.5	-76.8	32.0	32.0	[14]
D420	-49	-77.2	30.0	30.0	[14]
D500	-47	-77.7	29.0	29.0	[14]
D640	-41	-77.8	32.0	32.0	[14]
D	72.38	-69.49	24.0	24.0	[3,4]
D780	-36	-77.8	41.0	41.0	[14]
DAVI	78	-68.7	39.0	38.9	[8]
DEVL	161.9745	-81.4757	18	17.9	[9]
DIHI	159.48	-79.8491	21.4	21.0	[11]
DNTW	-107.7804	-76.4571	25.21	24.2	[9]
DOMEA	77.1047	-80.422	61.6	57.5	[13]
DRV	140	-66.8	28.0	27.6	[15]
DSS2	-59.5	-62.5	33.0	32.9	[16]
DSS6	-62.5	-64.7	35.0	34.4	[16]
DT154	77.0257	-74.5824	49.3	46.6	[13]
DUFK	-53.2007	-82.8619	38.4	37.4	[9]
E000	163.6175	-77.6262	20.3	20.0	[11]
E002	163.0078	-77.575	24.7	24.0	[11]
E004	162.0661	-77.4133	30.7	30.0	[11]
E006	161.6256	-77.3703	34.6	34.0	[11]
E008	160.5033	-77.2817	37.8	36.0	[11]
E010	160.086	-77.1847	39.0	37.2	[17,18]
E012	159.326	-77.0461	40.6	38.7	[18]
E018	157.224	-76.8234	40.7	38.6	[18]
E020	156.547	-76.7295	45.2	43.0	[18]
E024	155.238	-76.5394	45.6	43.4	[18]
E028	154.039	-76.3075	45.6	43.3	[18]
E030	153.379	-76.2511	45.5	43.2	[18]
EAGLE	77.0448	-76.4154	58.4	55.6	[13]
ERS11	-174.445	-77.12	17.5	18.0	[19]
ERS13	-173.637	-77.1217	17.5	18.0	[19]
ERS17	-172.027	-77.1217	18.5	19.0	[19]
ERS20	-170.813	-77.1217	19.5	20.0	[19]
ERS23	-169.61	-77.1217	21.5	22.0	[19]
ERS3	-178.583	-77.12	23.4	24.0	[19]
ERS5	-176.99	-77.1167	23.4	24.0	[19]
ESPZ	301.6	-63.7	37.0	36.4	[20]
FALL	-143.6284	-85.3066	24	23.7	[9]
FISH	162.5652	-78.9276	17	16.7	[9]
FISHER	67.39	-71.52	39.0	38.4	[8]
GM01	104.7291	-83.9858	34.5	31.2	[21]
GM02	97.5815	-79.4251	42.3	38.6	[21]
GM03	85.9439	-80.2169	56.0	52.1	[21]

GM04	61.1124	-82.9997	51.5	47.7	21
GM05	51.1588	-81.1841	50.2	46.4	21
GROV	75	-72.9	40.0	38.0	8
HOWD	-86.7694	-77.5285	37	35.5	9
ISDE	-134.9935	-80	28.0	27.4	10
J01-SP1	41.2	-70.2	41.0	40.0	22
J01-SP2	41.5	-69.8	41.0	40.0	22
J01-SP5	42.4	-69.25	41.0	40.0	22
J01-SP6	42.7	-69.08	41.0	40.0	22
J01-SP7	42.95	-68.7	41.0	40.0	22
J99-S1	40.06	-69.04	38.0	37.0	23
J99-S2	40.65	-69.06	40.0	39.0	23
J99-S3	41.3	-69.3	41.0	40.0	23
J99-S4	42	-69.6	42.0	41.0	23
J99-S5	42.6	-69.8	43.5	42.0	23
J99-S6	43.4	-70.2	45.0	43.0	23
JNCT	157.901	-76.9313	38.0	35.8	18
LONW	152.735	-81.3466	45	43.5	9
LT892	77.767	-71.6708	45.7	43.5	13
M450	165.4	-77.75	21.0	21.0	24
MAGL	162.4083	-76.1381	23.0	23.0	11
MBL	-130.2241	-78.093	25.0	23.4	10
MECK	-72.1849	-75.2807	26.5	25.4	9
MILR	156.2517	-83.3063	45	43.1	9
MINN	166.88	-78.5504	20.5	20.0	11
MPAT	-155.022	-78.0297	27.5	27.0	9
MTM	-100.0123	-79.496	21.0	19.0	10
MUC6-8	-11.065	-75.25	53.1	51.0	6
MZH	44.3	-70.1	44.0	42.0	23,25
N000	160.378	-76.0088	32.8	31.1	18
N020	155.818	-77.4678	40.5	38.2	18
N036	151.278	-78.5508	44.0	41.7	18
N044	148.616	-79.0692	47.0	44.7	18
N060	142.595	-80.0001	47.9	45.5	18
N076	135.434	-80.8062	48.0	45.5	18
N092	126.98	-81.4593	46.6	43.8	18
N100	122.61	-81.6525	45.5	42.6	18
N108	117.605	-81.8795	47.0	43.9	18
N116	112.571	-82.0098	45.1	41.9	18
N124	107.6406	-82.0745	47.9	44.5	21
N132	101.9534	-82.0751	45.3	41.9	21
N140	96.7692	-82.0086	49.3	45.7	21
N156	86.5045	-81.6726	46.3	42.4	21

N165	81.7604	-81.4084	56.5	52.5	[21]
N173	77.4736	-81.1122	59.2	55.2	[21]
N182	73.1898	-80.7363	57.8	53.7	[21]
N190	69.431	-80.3275	51.5	47.6	[21]
N198	65.9607	-79.8597	53.4	49.6	[21]
N206	62.8556	-79.3947	50.3	46.6	[21]
N215	59.9943	-78.9045	47.9	44.4	[21]
NOVO	11.835	-70.776	42.0	41.8	[6]
OND	-125.7358	-80.7456	28.0	26.9	[10]
P061	77.2238	-84.4996	46.1	42.6	[21]
P071	77.3347	-83.6465	43.0	39.4	[21]
P080	77.364	-82.8054	48.0	44.2	[21]
P116	77.0451	-79.5669	56.7	52.8	[21]
P124	77.657	-78.8718	58.9	55.3	[21]
PECA	-68.5527	-85.6124	37	35.5	[9]
PMSA	296	-64.8	40.0	39.8	[20]
**PMSA	-64	-64.8	36.0	36.0	[15]
REIN	72.55	-70.45	33.0	32.9	[8]
RIS51	-61	-74.7	33.0	33.0	[26]
RIS56	-55	-75.8	27.0	27.0	[26]
SAE33B	-12.5	-71.5	32.0	32.0	[6,27]
SAE33E	-7.2	-70.7	32.0	32.0	[6,27]
SAE34B	-10.5	-71	33.0	33.0	[6,27]
SAE34E	-4.8	-73.4	41.0	39.0	[6,27]; [1]
SBA	166.7573	-77.8491	21.0	21.0	[11]
SBA	166.757	-77.8491	21.0	21.0	[5]
SDM	-148.85	-81.6148	27.0	26.3	[10]
SILY	-125.966	-77.1332	32.8	30.7	[9]
SIPL	-148.9555	-81.6405	28.03	27.4	[9]
SNAA	-2.838	-71.671	40.0	39.2	[6]
SPA	0	-90	34.0	31.2	[10]
ST01	-98.7419	-83.2279	30.24	28.2	[9]
ST02	-109.1243	-82.069	34.24	32.5	[9]
ST03	-113.1504	-81.4065	26.53	24.9	[9]
ST04	-116.5782	-80.715	23.76	22.2	[9]
ST06	-121.8196	-79.3316	24.8	23.3	[9]
ST07	-123.7953	-78.6387	26.21	24.6	[9]
ST08	-125.5313	-77.9576	26.8	25.0	[9]
ST09	-128.4734	-76.5309	31.74	29.5	[9]
ST10	-129.7489	-75.8143	29.83	28.1	[9]
ST12	-123.816	-76.897	24.02	21.8	[9]
ST13	-130.5139	-77.5609	32.18	30.3	[9]
ST14	-134.0802	-77.8378	28.93	27.3	[9]

STC	-136.4061	-82.3575	31.0	30.5	10
SURP	-171.2018	-84.7199	26.5	26.1	9
THUR	-97.5606	-72.5301	24.1	23.9	9
TNV	164.12	-74.7	22.1	22.0	11
UPTW	-109.0396	-77.5797	22.39	21.1	9
VNDA	161.8456	-77.5139	35.6	35.0	11
**VNDA	161.846	-77.5139	35.0	34.4	5,17
**VNDA	161.853	-77.5172	35.3	34.7	18
VOSTOK	106.48	-78.28	30.0	26.5	28
**VOSTOK	106.48	-78.28	35.0	31.5	29
WA-AM	131.5	-64	18.0	21.0	30
WA-AN	132	-63.2	12.0	16.3	30
WA-BM	141	-65.1	16.0	18.7	30
WA-BN	141	-64.1	7.0	10.6	30
WA-BS	141	-65.6	23.0	24.1	30
WAIS	-111.7776	-79.4181	25.57	23.8	9
WEIGEL	-9.622	-74.275	44.0	42.5	6
WHIT	-104.3867	-82.6823	31.5	30.2	9
WILS	-80.5587	-80.0396	30	29.3	9
WM72	11.524	-72.144	50.0	47.4	6
WM73	11.562	-71.437	45.0	43.6	6
WM79	13.215	-72.04	51.0	48.6	6
WNDY	-119.4129	-82.3695	23.17	22.2	9
WRS10	-172.386	-77.0717	18.5	19.0	19
WRS11	-172.788	-77.0755	16.5	17.0	19
WRS12	-173.203	-77.0892	14.5	15.0	19
WRS14	-174.005	-77.1055	13.5	14.0	19
WRS17	-175.215	-77.1052	20.4	21.0	19
WRS21	-176.826	-77.1051	23.4	24.0	19
WRS2	-169.226	-77.0939	15.5	16.0	19
WRS25	-178.445	-77.1214	23.4	24.0	19
WRS29	-179.937	-77.1218	23.3	24.0	19
WRS3	-169.618	-77.1018	16.5	17.0	19
WRS4	-169.986	-77.1021	16.5	17.0	19
WRS6	-170.773	-77.0716	18.5	19.0	19
WRS7	-171.18	-77.0539	19.6	20.0	19
WRS8	-171.58	-77.0551	20.5	21.0	19
WRS9	-171.988	-77.0641	20.5	21.0	19
ZHSH	76.3727	-69.3747	38.3	38.3	13

Note: data sources are:

1 Hoffmann, M., Eckstaller, A., Jokat, W. & Miller, H. in *Workshop "East-West Antarctic Tectonics and Gondwana Breakup 60W to 60E" at ISAES IX meeting, September 8-12* (Potsdam, 2003).

2 Jokat, W., Ritzmann, O., Reichert, C. & Hinz, K. Deep Crustal Structure of the Continental Margin off the Explora Escarpment and in the Lazarev Sea, East Antarctica. *Mar Geophys Res* **25**, 283-304, doi:10.1007/s11001-005-1337-9 (2004).

3 Kolmakov, A. F., Mishenkin, B. P. & Solovyev, D. S. Deep seismic studies in East Antarctica. *Bulletin of Soviet Antarctic expedition*, 5-15 (1975).

4 Baranov, A. & Morelli, A. The Moho depth map of the Antarctica region. *Tectonophysics* **609**, 299-313, doi:http://dx.doi.org/10.1016/j.tecto.2012.12.023 (2013).

5 Bannister, S., Yu, J., Leitner, B. & Kennett, B. L. N. Variations in crustal structure across the transition from West to East Antarctica, Southern Victoria Land. *Geophysical Journal International* **155**, 870-880, doi:10.1111/j.1365-246X.2003.02094.x (2003).

6 Bayer, B., Geissler, W. H., Eckstaller, A. & Jokat, W. Seismic imaging of the crust beneath Dronning Maud Land, East Antarctica. *Geophysical Journal International* **178**, 860-876, doi:10.1111/j.1365-246X.2009.04196.x (2009).

7 Agostinetti, N. P., Amato, A., Cattaneo, M. & Di Bona, M. Crustal structure of northern Victoria Land from receiver function analysis. *Terra Antarctica* **11**, 5-14 (2004).

8 Reading, A. M. The seismic structure of Precambrian and early Palaeozoic terranes in the Lambert Glacier region, East Antarctica. *Earth and Planetary Science Letters* **244**, 44-57, doi:http://dx.doi.org/10.1016/j.epsl.2006.01.031 (2006).

9 Chaput, J. *et al.* The Crustal Thickness of West Antarctica. *J. Geophys. Res.*, submitted (2014).

10 Winberry, J. P. & Anandakrishnan, S. Crustal structure of the West Antarctic rift system and Marie Byrd Land hotspot. *Geology* **32**, 977-980, doi:10.1130/g20768.1 (2004).

11 Lawrence, J. F. *et al.* Crust and upper mantle structure of the Transantarctic Mountains and surrounding regions from receiver functions, surface waves, and gravity: Implications for uplift models. *Geochem. Geophys. Geosyst.* **7**, Q10011, doi:10.1029/2006gc001282 (2006).

12 Reading, A. M. The Seismic Structure of Wilkes Land/Terre Adelie, East Antarctica and Comparison with Australia: First Steps in Reconstructing the Deep Lithosphere of Gondwana. *Gondwana Research* **7**, 21-30, doi:http://dx.doi.org/10.1016/S1342-937X(05)70303-8 (2004).

13 Feng, M. *et al.* Crustal Thicknesses along the Traverse from Zhongshan to Dome A in Eastern Antarctica. *Chinese J. Polar Research* **26**, 177-185 (2014).

14 Leitchenkov, G. & Kudryavtzev, G. Structure and origin of the Earth's Crust in the Weddell Sea Embayment (beneath the Front of the Filehner and Ronne lee Shelves) from deep seismic sounding data. *Polarforschung* **67**, 143-154 (1997).

15 Kanao, M. & Shibutani, T. in *Seismic Waves - Research and Analysis* (ed Masaki Kanao) 237-252 (InTech, 2012).

16 Guterch, A., Grad, M., Janik, T., Perchuć, E. & Pajchel, J. Seismic studies of the crustal structure in West Antarctica 1979–1980—Preliminary results. *Tectonophysics* **114**, 411-429, doi:http://dx.doi.org/10.1016/0040-1951(85)90024-1 (1985).

17 Finotello, M., Nyblade, A., Julia, J., Wiens, D. & Anandakrishnan, S. Crustal Vp–Vs ratios and thickness for Ross Island and the Transantarctic Mountain front, Antarctica. *Geophysical Journal International* **185**, 85-92, doi:10.1111/j.1365-246X.2011.04946.x (2011).

18 Hansen, S. E. *et al.* Using S wave receiver functions to estimate crustal structure beneath ice

sheets: An application to the Transantarctic Mountains and East Antarctic craton. *Geochem. Geophys. Geosyst.* **10**, Q08014, doi:10.1029/2009gc002576 (2009).

19 Trey, H. *et al.* Transect across the West Antarctic rift system in the Ross Sea, Antarctica. *Tectonophysics* **301**, 61-74, doi:http://dx.doi.org/10.1016/S0040-1951(98)00155-3 (1999).

20 Vuan, A. Joint Inversion of Receiver Function of Teleseismic Body Waves and Local Group Velocity Dispersion Curves beneath ESPZ and PMSA Stations (Antarctic Peninsula). *Terra Antarctica* **8**, 49-54 (2001).

21 Hansen, S. E. *et al.* Crustal structure of the Gamburtsev Mountains, East Antarctica, from S-wave receiver functions and Rayleigh wave phase velocities. *Earth and Planetary Science Letters* **300**, 395-401, doi:10.1016/j.epsl.2010.10.022 (2010).

22 Miyamachi, H. *et al.* A refraction and wide-angle reflection seismic exploration in JARE-43 on the Mizuho Plateau, East Antarctica. *Polar Geoscience* **16**, 1-21 (2003).

23 Yoshii, K., Ito, K., Miyamachi, H. & Kanao, M. Crustal structure derived from refractions and wide-angle reflections in the Mizuho Plateau, East Antarctica. *Polar Geoscience* **17**, 112-138 (2004).

24 McGinnis, L. D., Bowen, R. H., Erickson, J. M., Allred, B. J. & Kreamer, J. L. East-West Antarctic boundary in McMurdo sound. *Tectonophysics* **114**, 341-356, doi:http://dx.doi.org/10.1016/0040-1951(85)90020-4 (1985).

25 Ikami, A. & Ito, K. Crustal structure in the Mizuho Plateau, East Antarctica, by a two-dimensional ray approximation. *Journal of Geodynamics* **6**, 271-283, doi:http://dx.doi.org/10.1016/0264-3707(86)90044-X (1986).

26 Jokat, W., Fechner, N. & Studinger, M. in *The Antarctic Region: Geological Evolution and Processes* (ed C.A. Ricci) 453-459 (Terra Antartica Publication, 1997).

27 Kudryavtzev, G. A., Butzenko, V. V. & Kadmina, I. N. in *Sixth international sysmposium on Antarctic earth sciences* 330-335 (National Institute for Polar Research, 1991).

28 Studinger, M. *et al.* Geophysical models for the tectonic framework of the Lake Vostok region, East Antarctica. *Earth and Planetary Science Letters* **216**, 663-677 (2003).

29 Isanina, E. V., Krupnova, N. A., Popov, S. V., Masolov, V. N. & Lukin, V. V. Deep structure of the Vostok Basin, East Antarctica as deduced from seismological observations. *Geotectonics* **43**, 221-225, doi:10.1134/s0016852109030042 (2009).

30 Eittreim, S. L. Transition from continental to oceanic crust on the Wilkes-Adelie margin of Antarctica. *Journal of Geophysical Research: Solid Earth* **99**, 24189-24205, doi:10.1029/94jb01903 (1994).

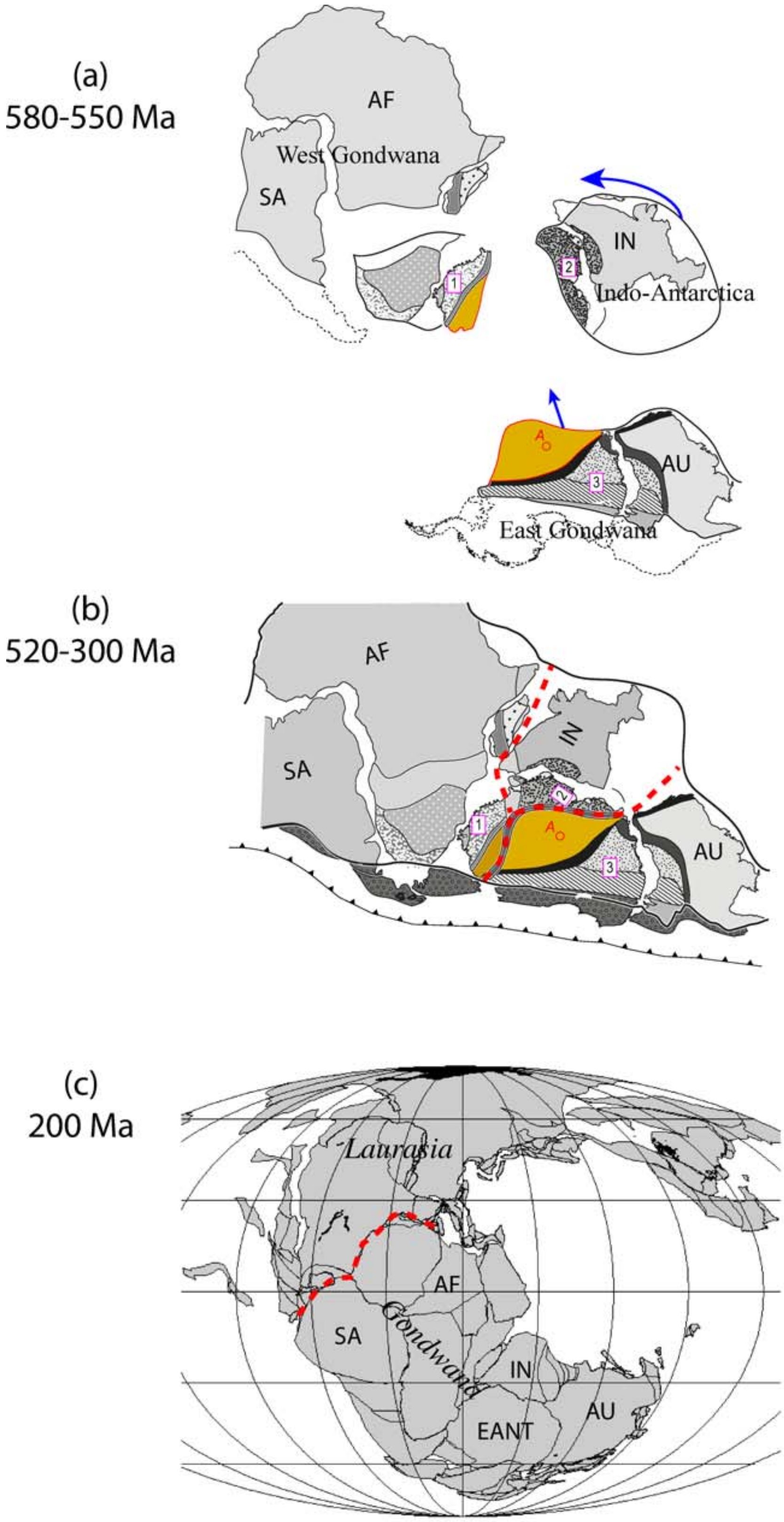
(a)
580-550 Ma
AF
West Gondwana
SA
1
IN
2
Indo-Antarctica
A
AU
3
East Gondwana
(b)
520-300 Ma
AF
SA
IN
2
1
A
3
AU
(c)
200 Ma
Laurasia
AF
SA
Gondwana
IN
AU
EANT

Figure S1

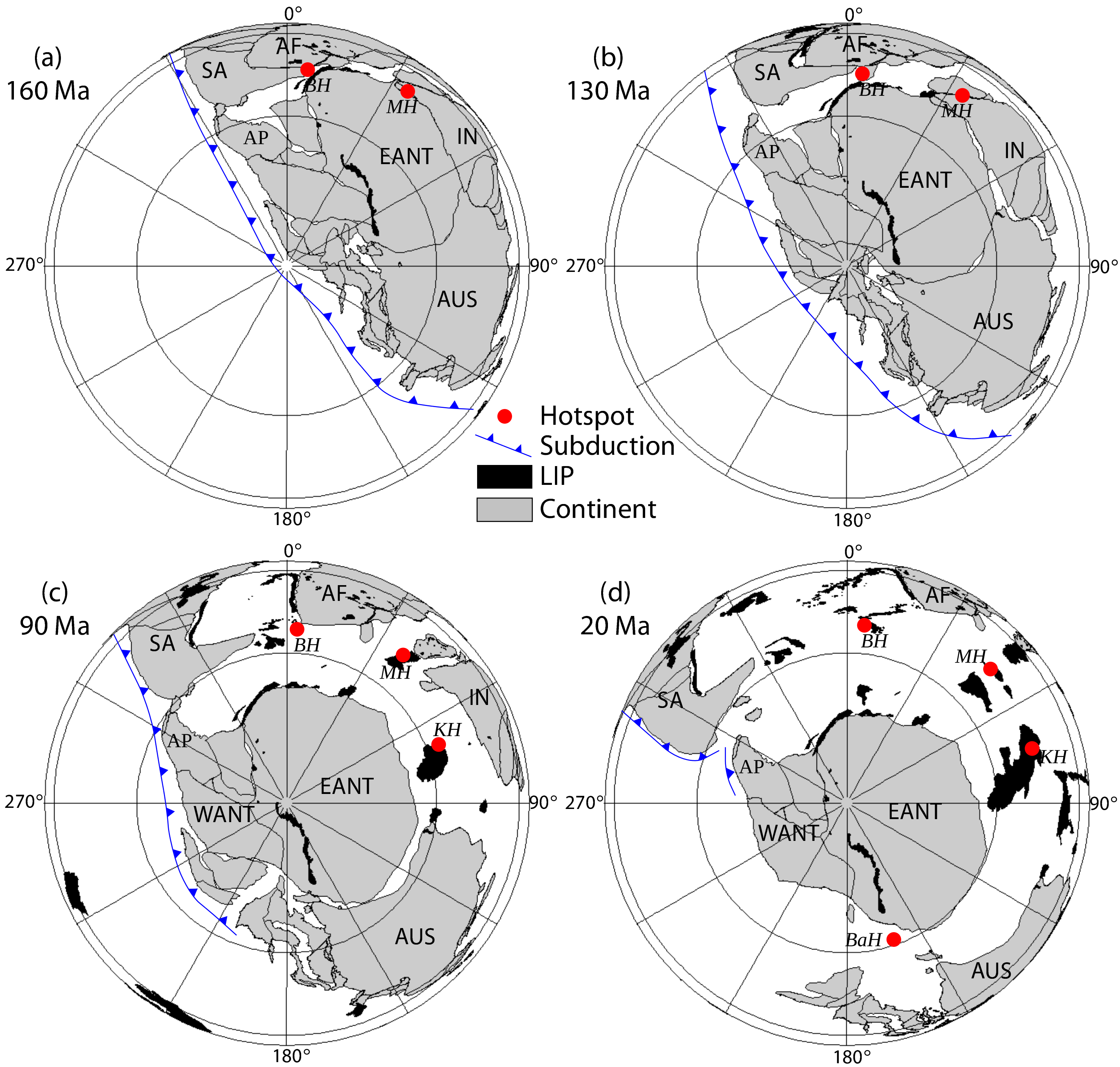

(a)
160 Ma
(b)
130 Ma
(c)
90 Ma
(d)
20 Ma
0°
90°
180°
270°
SA
AF
AP
EANT
WANT
IN
AUS
BH
MH
KH
BaH
Hotspot
Subduction
LIP
Continent

Figure S2

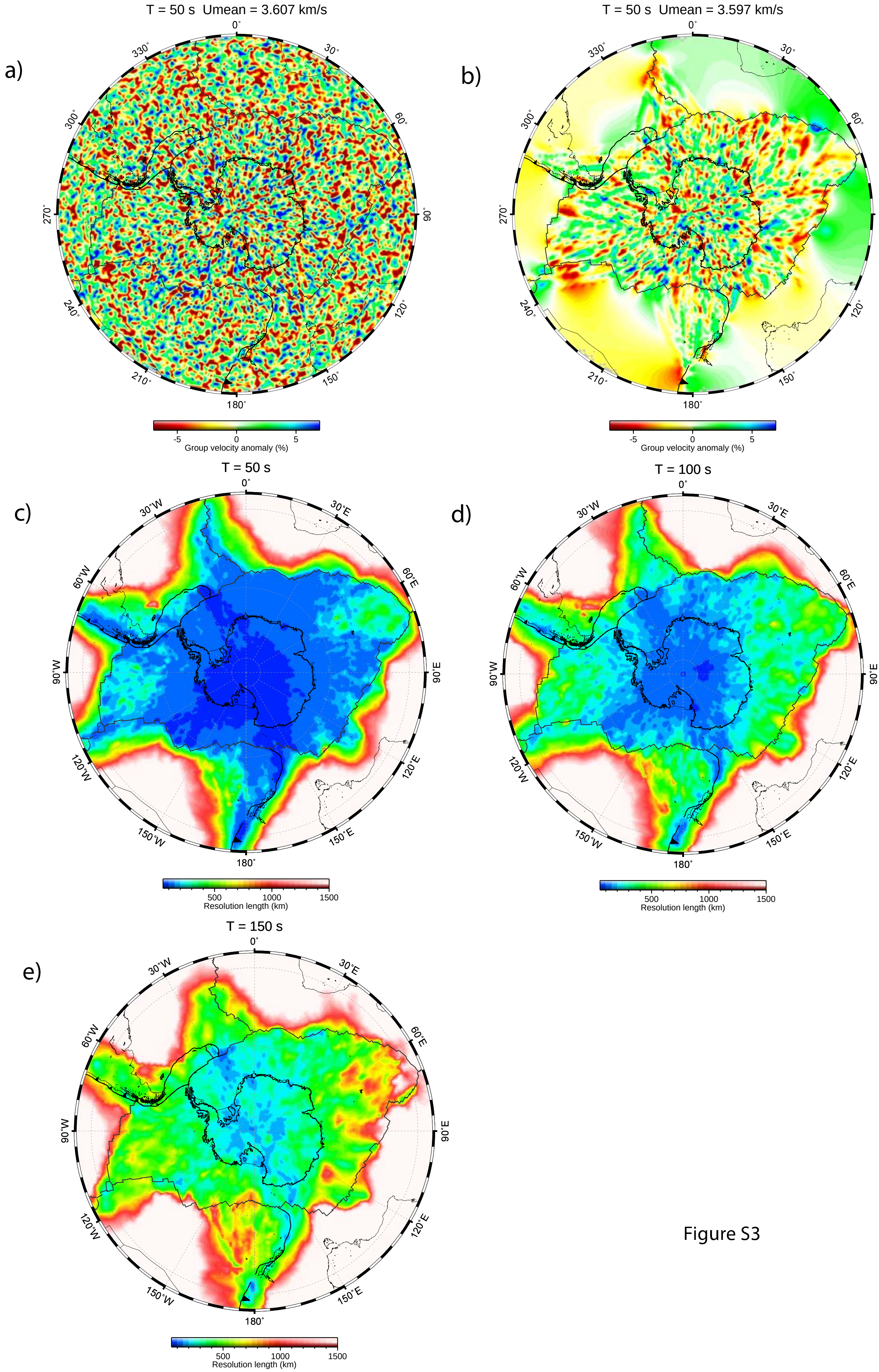
a)
T = 50 s Umean = 3.607 km/s
b)
T = 50 s Umean = 3.597 km/s
0°
30°
60°
90°
120°
150°
180°
210°
240°
270°
300°
330°
-5
0
5
Group velocity anomaly (%)
c)
T = 50 s
d)
T = 100 s
e)
T = 150 s
30°E
60°E
90°E
120°E
150°E
30°W
60°W
90°W
120°W
150°W
500
1000
1500
Resolution length (km)

Figure S3

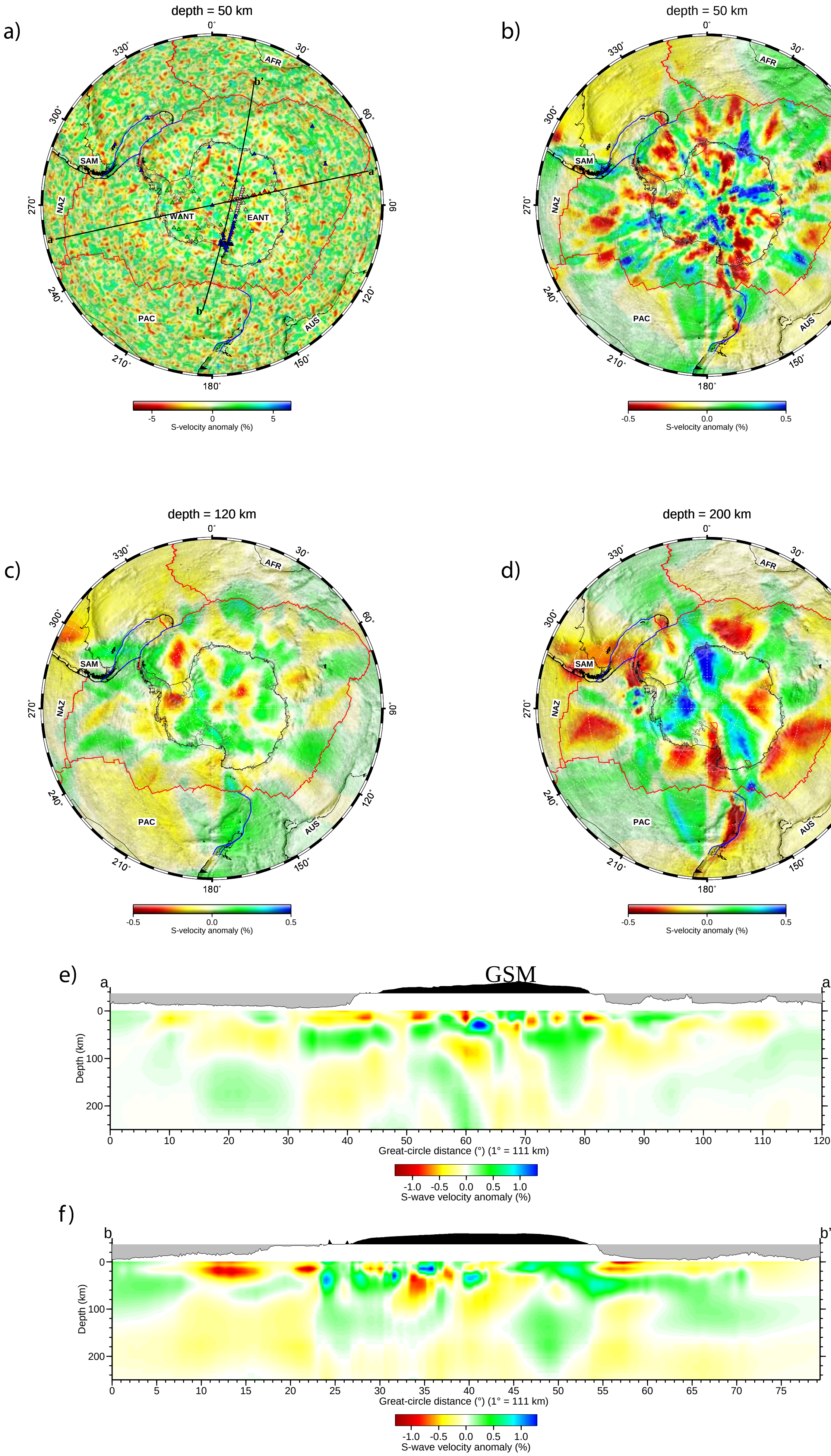

a)
depth = 50 km
b)
depth = 50 km
c)
depth = 120 km
d)
depth = 200 km
AFR
SAM
NAZ
PAC
AUS
WANT
EANT
S-velocity anomaly (%)
e)
GSM
a
a'
Depth (km)
Great-circle distance (°) (1° = 111 km)
S-wave velocity anomaly (%)
f)
b
b'
Depth (km)
Great-circle distance (°) (1° = 111 km)
S-wave velocity anomaly (%)

Figure S4

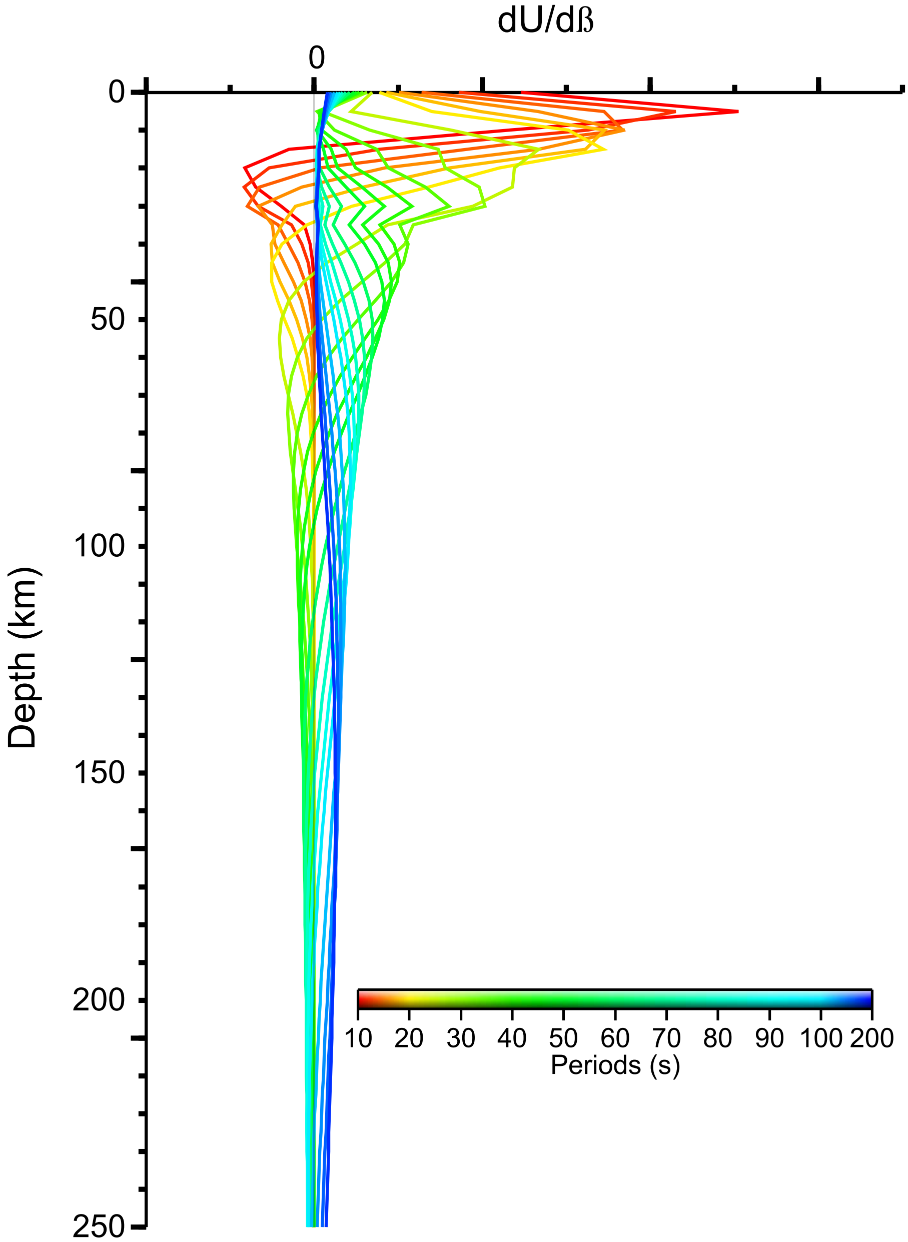

dU/dß
0
0
50
100
150
200
250
Depth (km)
10 20 30 40 50 60 70 80 90 100 200
Periods (s)

Figure S5

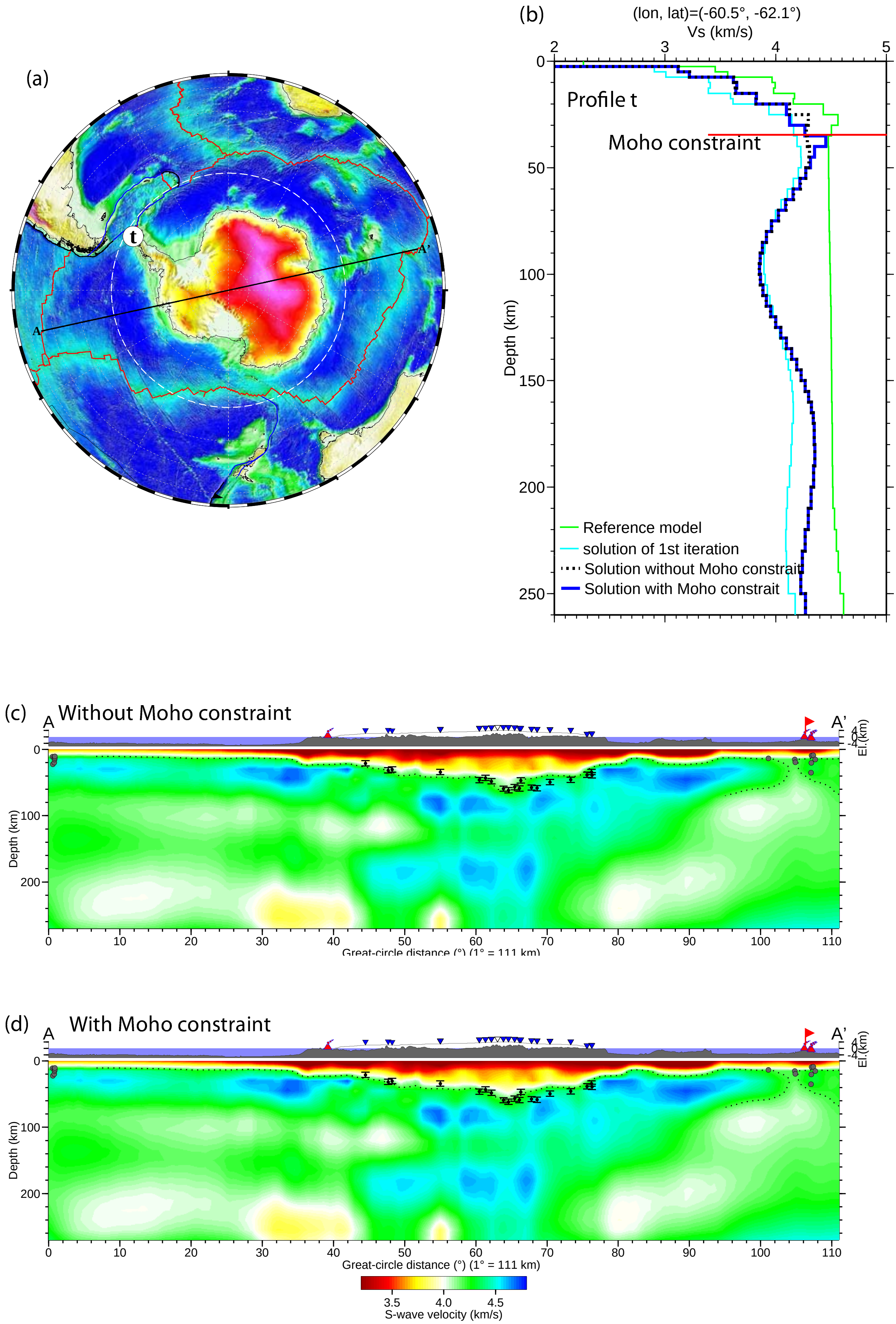
(a)
t
A
A'
(b)
(lon, lat)=(-60.5°, -62.1°)
Vs (km/s)
Depth (km)
Profile t
Moho constraint
Reference model
solution of 1st iteration
Solution without Moho constrait
Solution with Moho constrait
(c)
Without Moho constraint
Depth (km)
El.(km)
Great-circle distance (°) (1° = 111 km)
(d)
With Moho constraint
Depth (km)
El.(km)
Great-circle distance (°) (1° = 111 km)
S-wave velocity (km/s)

Figure S6

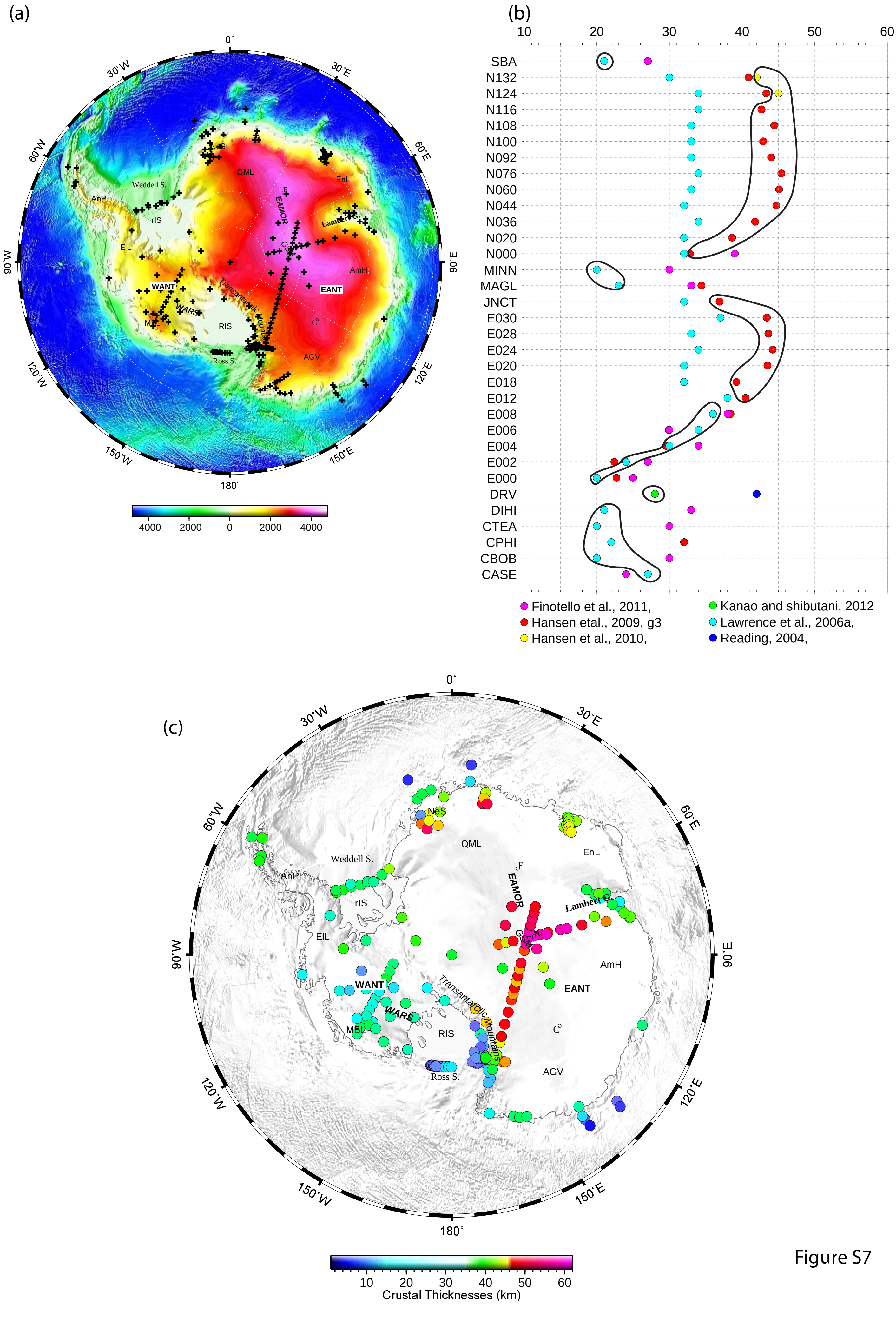

(a)
0°
30°W
30°E
60°W
60°E
90°W
90°E
120°W
120°E
150°W
150°E
180°
Weddell S.
AnP
rIS
EIL
WANT
WARS
MBL
RIS
Ross S.
NeS
QML
EAMOR
EnL
Lambert G.
AmH
EANT
Transantarctic Mountains
AGV
-4000
-2000
0
2000
4000
(b)
10
20
30
40
50
60
SBA
N132
N124
N116
N108
N100
N092
N076
N060
N044
N036
N020
N000
MINN
MAGL
JNCT
E030
E028
E024
E020
E018
E012
E008
E006
E004
E002
E000
DRV
DIHI
CTEA
CPHI
CBOB
CASE
Finotello et al., 2011,
Hansen etal., 2009, g3
Hansen et al., 2010,
Kanao and shibutani, 2012
Lawrence et al., 2006a,
Reading, 2004,
(c)
Crustal Thicknesses (km)
10
20
30
40
50
60

Figure S7